Modelling the Earth's core magnetic field under flow constraints

V. Lesur[1], I. Wardinski[1], S. Asari[1], B. Minchev[2,3] and M. Mandea[1,4]

[1] *Helmholtz Centre Potsdam, GFZ German Research centre for Geosciences, Telegrafenberg, 14473, Germany.*

[2] *Departement of Mathematics, Potsdam University, Potsdam, Germany.*

[3] *Now at Global Life, Allianz SE, 70178 Stuttgart, Germany.*

[4] *Now at Université Paris Diderot, Institut de Physique du Globe de Paris, Géophysique spatiale et planétaire, Paris, France*

Two recent magnetic field models, GRIMM and xCHAOS, describe core field accelerations with similar behavior up to Spherical Harmonic (SH) degree 5, but which differ significantly for higher degrees. These discrepancies, due to different approaches in smoothing rapid time variations of the core field, have strong implications for the interpretation of the secular variation. Furthermore, the amount of smoothing applied to the highest SH degrees is essentially the modeler's choice. We therefore investigate new ways of regularizing core magnetic field models. Here we propose to constrain field models to be consistent with the frozen flux induction equation by co-estimating a core magnetic field model and a flow model at the top of the outer core. The flow model is required to have smooth spatial and temporal behavior. The implementation of such constraints and their effects on a magnetic field model built from one year of CHAMP satellite and observatory data, are presented. In particular, it is shown that the chosen constraints are efficient and can be used to build reliable core magnetic field secular variation and acceleration model components

Key words: Geomagnetism, Core field modeling, Core flow modeling, Frozen-flux

1. Introduction

Following the launch of the magnetic survey satellites Oersted in 1999, and CHAMP in 2000, a global set of high quality

magnetic vector data is now available. Currently, this set spans nearly ten years and has led to time varying models of

the core magnetic field of unprecedented accuracy. One of the major achievements is the modeling of the magnetic field

Secular Acceleration (SA) i.e. the time evolution of the magnetic field Secular Variation (SV). Indeed, it is crucial to model

as accurately as possible the secular acceleration because it has a profound effect on the SV which in turn affects estimates

of the liquid outer core flow, just below the Core-Mantle Boundary (CMB). Properly describing the flow at the top of the

liquid outer core is essential as it is one key piece of information to understand the dynamics of the core, with implications

for other physical process such as long timescale changes in the length of the day.

The secular acceleration is modeled in the available core magnetic field models with time variations described by cubic (or higher order) B-splines. For example this is the case for the CM4 (Sabaka et al., 2004), GUFM (Jackson et al., 2000) or CALS7K (Korte and Constable, 2004) models. However, these models, that are needed to describe relatively long term variations of the Earth's core magnetic field, have been built with relatively few data per year, and therefore have been strongly smoothed in time.

Extracting the acceleration information from geomagnetic observatory and satellite data is a challenging task. Only recently has it become clear that this is possible for magnetic field models spanning only a few years. First attempts have been made by Lesur et al. (2005), Maus et al. (2005), Olsen et al. (2005), but their SA models do not agree. The CHAOS model (Olsen et al., 2006) presents a more realistic SA but the use of cubic B-splines to parameterize in time the core magnetic field precludes its continuous mapping. This problem has been addressed in the GRIMM model (Lesur et al., 2008) where order five B-splines have been used, leading to the first continuous time dependent model of the SA that is believed to be reasonably accurate up to Spherical Harmonic (SH) degree 5 or 6. A recent extension of the CHAOS model, named xCHAOS (Olsen and Mandea, 2008, version 03c-08, personal communication), although built using completely different data selection techniques, has SA agreeing with the very long spatial wavelengths of that computed from GRIMM. Typically, the two models present strong similarities in SA up to SH degrees 4 or 5. For higher SH degrees however, the two SA models are radically different (See figure 1). The data set and the applied processing do not resolve the acceleration signal well and there is not even agreement as to what the shape of the SA power spectrum should be. Usually, during the modeling process, the SA is controlled through a rather simple regularization imposing smooth behavior in space and time. Indeed, it is rather difficult to estimate what smoothness or magnitude the SA should have. Therefore, it is necessary to seek for alternative ways of regularizing the magnetic field models in order to improve our understanding of the SA at SH degrees higher than 5.

In this manuscript we present our approach to model both the core magnetic field and the flow on the core surface simultaneously. More specifically, a core magnetic field model, built to fit a magnetic data set, is co-estimated together with a flow model using the radial diffusionless induction equation (hereafter the FF-equation). Constraints are applied exclusively on the flow model in order to obtain the best possible core field model. At a glance, it is not obvious why smoothing the flow is preferable to smoothing the field. Both regularization techniques are, however, likely to single out a possible mechanism (i.e. diffusion or advection) for the SV generation in the core. Here, by using the FF-equation we favor an advective process, and show that smoothing in time the field is likely to favor diffusion. Indeed, it is well-known that some diffusion must exist, and therefore an advective process, even if dominant, cannot be the exclusive source of the SV. To avoid this pitfall, we impose the diffusionless hypothesis (hereafter the FF-hypothesis) in a weak form, such that the data
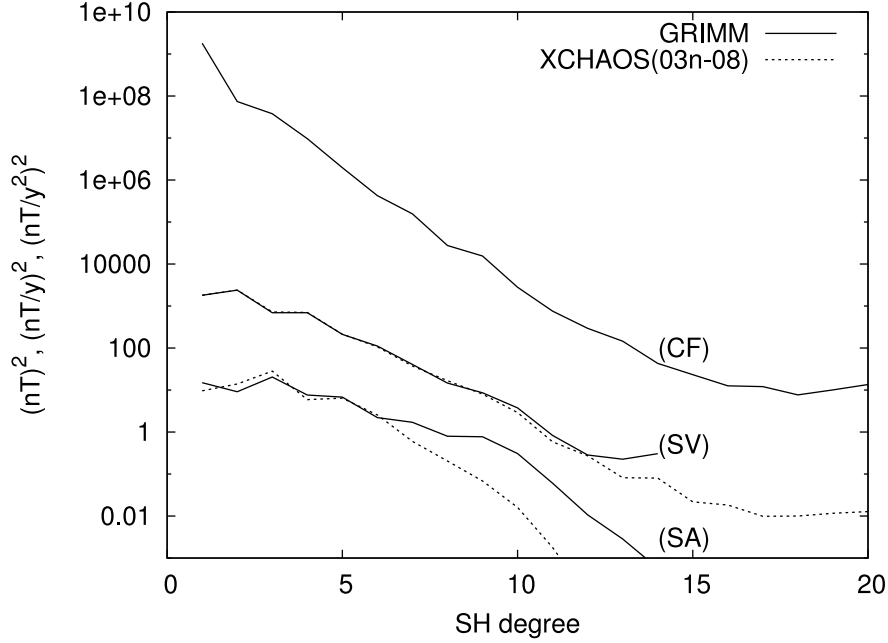
Fig. 1. Comparison of power spectra between the GRIMM and xCHAOS static core field (CF), secular variation (SV) and acceleration (SA). The spectra
    are all calculated at the Earth's reference radius and for the year 2005.4.

set can always be properly fitted.

The idea of imposing the FF-hypothesis on a core field model has already been used for example by Bloxham and Gubbins

(1986) and Jackson et al. (2007). These authors require the magnetic flux to be constant in time over areas on the CMB

defined by null flux curves at different epochs. Our approach is different because we co-estimate the flow and the field

and therefore impose some constraints on the flow. Furthermore, the FF-hypothesis is applied continuously in time. Closer

to our approach is that of Waddington et al. (1995) where observatory data are fit by parameterizing the flow on the core

surface. Their work is sometimes seen as an early attempt of a data assimilation technique where the physical model for

the flow evolution is replaced by an hypothesis of steady flow. Beggan and Whaler (2009) also used a steady flow model,

combined with Kalman filtering, to forecast change of the magnetic core field. In our case the flow is allowed to vary in

time and the difference with assimilation techniques is that evolution equations for the flow are not introduced. On the other

hand, the new assimilation techniques recently developed for the magnetic field modeling are not yet based on real data but

only on models (Liu et al., 2007; Fournier et al., 2007). We also note that the approach we follow in this study has been

independently suggested, in their conclusion, by Whaler and Holme (2007).

Here, our main goal is to investigate how well one can control a core field model by applying constraints on the co-

estimated flow model. The methodology is tested on a vector CHAMP satellite and observatory data set spanning only one

year. By using such a short time span, we make sure that the constraints applied on the flow have an obvious effect on the

field model. On the other hand, the resulting core field model cannot be of the same quality as models recently derived

from the full set of available satellite and observatory data, such as GRIMM (Lesur et al., 2008) and xCHAOS (Olsen and

Mandea, 2008). In particular, as for other models built from short time span data sets (see for example Olsen (2002)), the

acceleration cannot be accurately modeled. We also impose some strong restrictions on the flow by first truncating the flow

model to a relatively low SH degree, and second, choosing the same temporal representation for the flow coefficients and for

the Gauss coefficients. As for the field models, the obtained flow model cannot be of the same quality of recently published

models, nevertheless, it is of sufficient quality for the purpose of this study.

The manuscript is organized as follow. The necessary assumptions of the problem and the implementation details are

presented in the next section. In the third section the application to the CHAMP satellite and observatory vector data is

presented. The fourth section is dedicated to evaluating the effect of the regularization on the field and flow models. Finally,

in the fifth section, the obtained magnetic field, the fit to the data, and the flow models are discussed and compared with the

GRIMM magnetic field model.

2.   Theoretical background

Let us first consider a (column) vector $\mathbf{d}$ made of N vector magnetic field measurements d_i at $(t_i, \theta_i, \phi_i, r_i)$ where t ,

θ, ϕ and r are the time, co-latitude, longitude and radius respectively and $i = 1, 2, \cdots, N$. For simplicity, we assume in

this section that only the core field contributes to these measurements. These measurements are made above the Earth's

surface and are contaminated by some noise. The Earth's surface is away from the core magnetic field sources and therefore

the observations can be well approximated by a field model $B(t, \theta, \phi, r)$ that is the negative gradient of a potential, itself

solution of the Laplace's equation:

$$B(t, \theta, \phi, r) = -\nabla V(t, \theta, \phi, r), \tag{1}$$

$$\nabla^2 V(t, \theta, \phi, r) = 0. \tag{2}$$

To derive a flow model at the core surface, we neglect the effect of mantle conductivity on a temporal variation of the

core field, and therefore assume that the core field model determined at the observation radius can be directly downward

continued to the CMB. Further it is assumed that the contributions to the temporal variations of the core field $\partial_t B$ are first

the advection of the magnetic field line of force by the liquid outer core flow and second the diffusion of the field. Following

Roberts and Scott (1965) (see also Holme (2007)) we write:

$$\partial_t B = \nabla \times (U \times B) + \eta \nabla^2 B \tag{3}$$

where U is the flow in the liquid outer core. In this equation the parameter $\eta = \frac{1}{\sigma \mu}$ is proportional to the inverse of the

core conductivity and is therefore very small. As a consequence, for SV on decadal time scales and processes on large

spatial scales ($> 10^3$km) the second term on the right hand side of equation 3 can be neglected. This approximation is called the Frozen-Flux hypothesis (i.e. FF-hypothesis, see Roberts and Scott (1965) for the original justification of this approximation). Under this approximation, and assuming that the CMB is a spherical surface, the radial component of equation 3 becomes the radial diffusionless induction equation (i.e. the FF-equation):

$$\partial_t B_r = -\nabla_h \cdot (U_h B_r), \tag{4}$$

where U_h is the vector flow tangential to the spherical surface on the top of the core (the radial flow component necessarily vanishes at the core surface), B_r and $\partial_t B_r$ are the radial component of the core field model and its SV at the CMB and $\nabla_h = \nabla - \hat{r}\partial_r$ is the tangential gradient on the sphere. The tangential components of the magnetic field are discontinuous across the CMB and therefore are not used here to derive the core flow (Jault and Le Mouël, 1991).

2.1 The discrete problem

At the CMB, the magnetic field model solution of equations 1, 2 can be parameterized using SHs:

$$B(t, \theta, \phi, r) = -\nabla\{c\sum_{l=1}^{L_B}\sum_m (\frac{c}{r})^{(l+1)}g_l^m(t)Y_l^m(\theta, \phi)\} \tag{5}$$

$$g_l^m(t) = \sum_{i=1}^{N_t} g_{li}^m \psi_i(t) \tag{6}$$

where $c = 4385$km is the Earth's core reference radius, $Y_l^m(\theta, \phi)$ are the Schmidt semi-normalized SHs. We use the convention that negative orders, $m < 0$, are associated with $\sin(|m|\phi)$ terms whereas null or positive orders, $m \geq 0$, are associated with $\cos(m\phi)$ terms. The N_t basis functions in time $\psi_i(t)$ are polynomials of maximum degree $N_t - 1$. The sum in the right hand side of equation 5 goes up to degree L_B and therefore the magnetic field model is defined by $(L_B(L_B + 2)N_t)$ Gauss coefficients g_{li}^m. These Gauss coefficients can be estimated by solving the linear system:

$$\mathbf{d} = \mathbf{A} \cdot \mathbf{g} + \mathbf{e}_d \tag{7}$$

where the elements of the $N \times (L_B(L_B + 2)N_t)$ matrix $\mathbf{A}$ are derived from equations 5, 6 and $\mathbf{g} = [g_{li}^m]_{\{l,m,i\}}$ is the vector of Gauss coefficients. The vector $\mathbf{e}_d$ is introduced to account for the noise in the data. We recall that N is the number of data values. In the present study $L_B = 14$ and $N_t = 5$.

In order to re-write equation 4 as a set of linear equations, the usual parameterization of the flow at the core surface is used (see for example Whaler (1986); Bloxham (1988)). The flow at the core surface is described as the sum of poloidal and toroidal flows, each of these flows being parameterized using SHs:

$$U_h(t, \theta, \phi, r) = \nabla_h \times (\vec{r}T) + \nabla_h(rS) \tag{8}$$

$$T = \sum_{l=1}^{L_F}\sum_m t_l^m(t)Y_l^m(\theta, \phi)$$
$$S = \sum_{l=1}^{L_F}\sum_m s_l^m(t)Y_l^m(\theta, \phi) \tag{9}$$

$$t_l^m(t) = \sum_{i=1}^{N_t} t_{li}^m \psi_i(t)$$
$$s_l^m(t) = \sum_{i=1}^{N_t} s_{li}^m \psi_i(t). \tag{10}$$

Here we note that the same basis functions are used to expand the magnetic field model and the flow model in time.

The radial component of the core magnetic field model is given by:

$$B_r(t, \theta, \phi, r) = \sum_{l,m} (l+1) g_l^m(t) (\frac{c}{r})^{(l+2)} Y_l^m(\theta, \phi). \tag{11}$$

Inserting equations 8 and 11 into equation 4, then multiplying both sides by $Y_l^m(\theta, \phi)$ and finally integrating over the sphere leads to:

$$\partial_t g_l^m(t) = \frac{(2l+1)}{4\pi c(l+1)} \sum_{l',m',l'',m''} (l'+1) g_{l'}^{m'}(t) \{ s_{l''}^{m''}(t) \frac{l(l+1)+l''(l''+1)-l'(l'+1)}{2} G_{l''l',m''m'}^{l,m}$$
$$+ t_{l''}^{m''}(t) \, S_{l''l',m''m'}^{l,m} \} \tag{12}$$

where $G_{l''l',m''m'}^{l,m}$ and $S_{l''l',m''m'}^{l,m}$ are the Gaunt and Elsasser's integrals respectively.

$$G_{l''l',m''m'}^{l,m} = \int_\Omega Y_{l''}^{m''}(\theta, \phi) Y_{l'}^{m'}(\theta, \phi) Y_l^m(\theta, \phi) d\omega$$
$$S_{l''l',m''m'}^{l,m} = \int_\Omega \{ \partial_\theta Y_{l''}^{m''}(\theta, \phi) \partial_\phi Y_{l'}^{m'}(\theta, \phi) - \partial_\phi Y_{l''}^{m''}(\theta, \phi) \partial_\theta Y_{l'}^{m'}(\theta, \phi) \} \frac{Y_l^m(\theta, \phi)}{\sin \theta} d\omega. \tag{13}$$

We define the matrix $\dot{\mathbf{\Psi}}(t)$ made of the $\partial_t \psi_i(t)$ and padded with zeros such that:

$$\dot{\mathbf{\Psi}}(t) \cdot \mathbf{g} = \begin{bmatrix} \partial_t g_1^0(t) \\ \vdots \\ \partial_t g_{L_B}^{L_B}(t) \\ 0 \\ \vdots \\ 0 \end{bmatrix}. \tag{14}$$

The number of elements of this vector is $(L_F + L_B)(L_F + L_B + 2)$ where L_B and L_F are the upper-bounds of the summations in equations 5 and 9. This number corresponds to the Gaunt and Elsasser's integral exclusion rule (see for example Moon (1979)), and the matrix formulation for equation 12 becomes:

$$\dot{\mathbf{\Psi}}(t) \cdot \mathbf{g} = \mathbf{A}_g(t) \cdot \mathbf{u} + \mathbf{e}_t \quad \text{where} \quad \mathbf{u} = \begin{bmatrix} t_{li}^m \\ s_{li}^m \end{bmatrix}_{\{l,m,i\}}. \tag{15}$$

The elements of the time-dependent matrice $\mathbf{A}_g(t)$ are derived from equation 12 and the truncation error $\mathbf{e}_t$ is introduced because $\partial_t g_l^m(t)$ is known only up to SH degree L_B leading to only $L_B(L_B+2)$ non-zero elements in the vector $\dot{\mathbf{\Psi}}(t) \cdot \mathbf{g}$. The dimension of vector $\mathbf{u}$ is $2L_F(L_F+2)N_t$. This is also the number of columns of $\mathbf{A}_g(t)$. In this work we set $L_B = L_F = 14$.

An alternative way of presenting the equations 12, 15 is to define the matrix $\mathbf{A}_u(t)$ such that $\mathbf{A}_g(t) \cdot \mathbf{u} = \mathbf{A}_u(t) \cdot \mathbf{g}$ and then equations 12, 15 become:

$$0 = (\mathbf{A}_u(t) - \dot{\mathbf{\Psi}}(t)) \cdot \mathbf{g} + \mathbf{e}_t. \tag{16}$$

As for $\mathbf{A}_g(t)$, the $\mathbf{A}_u(t)$ matrix elements are derived from equation 12. The matrix $\mathbf{A}_u(t)$ has only $L_B(L_B+2)N_t$ columns but the same number of rows as $\mathbf{A}_g(t)$. We have verified that for non-vanishing flow the matrix $(\mathbf{A}_u(t) - \dot{\mathbf{\Psi}}(t))$ is not singular, therefore if $\mathbf{e}_t = 0$, the only solution of equation 16 is the trivial solution $\mathbf{g} = 0$. This is clearly in contradiction with the solution of equation 7 and comes from the fact that the parameterization 5, 6, 9 and 10, for the core field and for the flow respectively, are not compatible with the FF-equation 4. This inconsistency has also been pointed out by Bloxham (1988). Elements of the proof are given in the appendix, and we simply note here that a small "representation" error $\mathbf{e}_r$ should be considered for both equations 15 and 16. The relative importance of $\mathbf{e}_t$ and $\mathbf{e}_r$ is discussed in sub-section 2.3.

2.2 Solving for the Gauss coefficients

To model the core magnetic field alone from a data set, the Gauss coefficients defined in equation 5 have to be estimated from the discrete linear system 7. This linear system is usually over-determined and therefore solved by least squares i.e the vector $\mathbf{g}$ is estimated such that it minimizes the functional Φ_0 defined by:

$$\Phi_0 = (\mathbf{d} - \mathbf{A} \cdot \mathbf{g})^{\mathrm{T}} \cdot \mathbf{W}^d \cdot (\mathbf{d} - \mathbf{A} \cdot \mathbf{g}) \tag{17}$$

where the superscript T denotes the transpose and the matrix $\mathbf{W}^d$ is a matrix of weights that is described in the next sub-section 2.3.

In order to co-estimate the core field and flow models, the linear systems 7 and 15 are solved simultaneously. The set of Gauss and flow coefficients solutions of equations 7 and 15 are obtained by least squares i.e. the Gauss and flow coefficients $[g_{li}^m, s_{li}^m, t_{li}^m]_{\{l,m,i\}}$ are estimated such that they minimize the functional Φ defined by:

$$\Phi = \Phi_0 + \lambda_1 \Phi_1$$
$$\Phi_1 = \sum_{t_i} \mathrm{w}_i^t \, (\mathbf{A}_g(t_i) \cdot \mathbf{u} - \dot{\mathbf{\Psi}}(t_i) \cdot \mathbf{g})^{\mathrm{T}} \cdot \mathbf{W}^{\dot{g}} \cdot (\mathbf{A}_g(t_i) \cdot \mathbf{u} - \dot{\mathbf{\Psi}}(t_i) \cdot \mathbf{g}) \tag{18}$$

where λ_1 is a scalar parameter that has to be adjusted and Φ_0 is defined in equation 17. If the elements of the diagonal weight matrix $\mathbf{W}^{\dot{g}}$ are defined by $\mathrm{w}_l^{\dot{g}} = \frac{4\pi(l+1)^2}{(2l+1)}$, then the functional Φ_1 is the discrete equivalent of the integral:

$$\int_{\mathcal{T}} \int_{\Omega} |\dot{B}_r(t_i) + \nabla_h \cdot (U_h B_r)|^2 \, d\omega \, dt. \tag{19}$$

However, in this work, the elements of $\mathbf{W}^{\dot{g}}$ have a more complex dependence on the SH degree. Their derivation is described in the next sub-section 2.3. In equation 18, the summation in Φ_1 is the integration over time. The sampling points t_i and the associated weights w_i^t are those of Gaussian integration rules and are such that the products of the different time-dependent terms are integrated exactly over the time span of the core field model $\mathcal{T}$.

Because $\mathbf{A}_g(t_i)$ in the functional Φ_1 depends on the Gauss coefficients g_{li}^m and is multiplied by $\mathbf{u}$, this optimization problem is clearly non-linear. We therefore re-write equation 18 explicitly as an iterative process. Consider $\mathbf{u}_k$ and $\mathbf{g}_k$, the kth estimates of the solution $\mathbf{u}$ and $\mathbf{g}$ respectively. Let us call $\mathbf{A}_{uk}(t)$ and $\mathbf{A}_{gk}(t)$ their corresponding matrices. We want to

estimate $\delta\mathbf{u}$ and $\delta\mathbf{g}$ that minimize:

$$\widetilde{\Phi} = \widetilde{\Phi}_0 + \lambda_1 \widetilde{\Phi}_1$$

$$\widetilde{\Phi}_0 = (\delta\mathbf{d} - \mathbf{A} \cdot \delta\mathbf{g})^{\mathsf{T}} \cdot \mathbf{W}^d \cdot (\delta\mathbf{d} - \mathbf{A} \cdot \delta\mathbf{g})$$

$$\widetilde{\Phi}_1 = \sum_{t_i} \mathrm{w}_i^t \left(\delta\dot{\boldsymbol{\Psi}}(t_i) + (\mathbf{A}_{uk}(t_i) - \dot{\boldsymbol{\Psi}}(t_i)) \cdot \delta\mathbf{g} + \mathbf{A}_{gk}(t_i) \cdot \delta\mathbf{u}\right)^{\mathsf{T}} \tag{20}$$

$$\cdot \mathbf{W}^{\dot{\mathbf{g}}} \cdot \left(\delta\dot{\boldsymbol{\Psi}}(t_i) + (\mathbf{A}_{uk}(t_i) - \dot{\boldsymbol{\Psi}}(t_i)) \cdot \delta\mathbf{g} + \mathbf{A}_{gk}(t_i) \cdot \delta\mathbf{u}\right)$$

where $\delta\mathbf{d} = \mathbf{d} - \mathbf{A} \cdot \mathbf{g}_k$, $\delta\dot{\boldsymbol{\Psi}}(t) = (\mathbf{A}_{uk}(t) - \dot{\boldsymbol{\Psi}}(t)) \cdot \mathbf{g}_k$, $\mathbf{u}_{k+1} = \mathbf{u}_k + \delta\mathbf{u}$ and $\mathbf{g}_{k+1} = \mathbf{g}_k + \delta\mathbf{g}$. This optimization problem, that is now linear in $\delta\mathbf{u}$ and $\delta\mathbf{g}$, can be solved but the iterative process is unlikely to converge unless some constraints are applied on the flow model. Indeed, it is well known that the problem is ill-posed for the flow (Holme, 2007). For example, if $L_F \geq L_B$, it is always possible to define an average toroidal flow following the iso-contours of the average radial component of the core field model. Such a flow does not generate any SV by advection. In order to obtain the best possible magnetic field model fitting the data and simultaneously reducing the null space for the flow, two types of constraints are considered:

- First, the flow model can be forced to have a convergent spectrum. The flow is then required to minimize Bloxham's "strong norm" (Bloxham, 1988; Jackson, 1997),

$$\lambda_{2B} \int_{\mathcal{T}} \int_{\Omega} |\nabla_h(\nabla_h \cdot U_h)|^2 + |\nabla_h(\hat{r} \times \nabla_h \cdot U_h)|^2 \, d\omega \, dt. \tag{21}$$

Another option is to minimize a weaker norm (Gillet et al., 2009),

$$\lambda_{2W} \int_{\mathcal{T}} \int_{\Omega} |\nabla_h \cdot U_h|^2 + |\hat{r} \times \nabla_h \cdot U_h|^2 \, d\omega \, dt. \tag{22}$$

The first and second terms in the integral 22 measure the amount of up/downwelling and the radial vorticity respectively. The damping parameters λ_{2B} and λ_{2W} controls to what extent the flow follows these constraints.

- Second the flow model is chosen such that it varies smoothly in time, namely:

$$\lambda_3 \int_{\mathcal{T}} \int_{\Omega} |\dot{U}_h|^2 d\omega \, dt \tag{23}$$

where λ_3 is the associated damping parameter and $\dot{U}_h$ denotes the flow time derivative. We expect such a constraint to efficiently regularize the inverse problem as in the limit of a constant flow there is a unique flow solution of the FF-equation (Voorhies and Backus, 1985). We also expect that minimizing equation 23 constrains efficiently the secular acceleration.

2.3   Errors and weight matrices

In the inverse problem 17, that consists of estimating a core field model from a data set, the weight matrix W^d depends, at first, on the estimated data accuracy and also on the data density. The matrix is then updated during the iterative least

squares inversion process used to derived the model. The data errors are assumed to be uncorrelated so the weight matrix is diagonal.

When the field and the flow are co-estimated, the functional Φ_1 and the diagonal weight matrix $\mathbf{W}^{\dot{g}}$ are introduced (equation 18). The $\mathbf{W}^{\dot{g}}$ matrix elements result from three different contributions, namely: the surface integration weights in equation 19, the representation errors $\mathbf{e}_r$ and the truncation errors $\mathbf{e}_t$ (see sub-section 2.1 for these error definitions). At a given instant t_i, the integral over the CMB of the squared radial component of the SV is given by:

$$\int_{\Omega} |\dot{B}_r(t_i)|^2 d\omega \;=\; \sum_{l,m} \frac{4\pi(l+1)^2}{(2l+1)} (\dot{g}_l^m(t_i))^2, \tag{24}$$

where the Gauss' coefficients are defined at the CMB (see equations 5, 6). Accordingly, integration weights for a given SH degree l are:

$$\frac{(l+1)^2}{(2l+1)}. \tag{25}$$

For SH degrees less than or equal to L_B, we assume that the representation error $\mathbf{e}_r$ dominates the truncation error $\mathbf{e}_t$. This latter error is simply ignored (but see the remark at the end of the sub-section). We set the variance at SH degree l of the representation errors proportional to:

$$V_l(e_r) \propto \frac{\dot{R}_l}{(l+1)(2l+1)} \tag{26}$$

where $\dot{R}_l = (l+1)\sum_m (\dot{g}_l^m)^2$ is the estimated power spectrum of a SV model defined at the CMB. This corresponds to the idea that the representation errors at CMB are simply proportional to the SV Gauss coefficients.

For SH degrees larger than L_B, the SV model is undefined giving rise to the truncation errors $\mathbf{e}_t$. The representation error $\mathbf{e}_r$ is then ignored. At the observational radius $a = 6371.2$km, the power spectrum of the SV at SH degrees larger than L_B is smaller than $0.5(\text{nT/y})^2$. We use this upper-bound as an estimate of the truncation error variance at SH degree l:

$$V_l(e_t) \propto \frac{0.5}{(l+1)(2l+1)} \left(\frac{a}{c}\right)^{2l+4}. \tag{27}$$

This variance is clearly over-estimated which, in the inverse problem defined by equation 18, is nearly equivalent to neglecting all equations above SH degrees L_B in the linear systems 15 and 16.

The elements of the diagonal weight matrix $\mathbf{W}^{\dot{g}}$ that correspond to the Gauss coefficients of SH degree $l \leq L_B$, are therefore given by:

$$\mathrm{w}_l^{\dot{g}} \propto \frac{(l+1)^2}{(2l+1)} \frac{(l+1)(2l+1)}{\dot{R}_l}, \tag{28}$$

for a SH degree $l > L_B$ the weights are given by:

$$\mathrm{w}_l^{\dot{g}} \propto \frac{(l+1)^2}{(2l+1)} \frac{(l+1)(2l+1)}{0.5} \left(\frac{c}{a}\right)^{2l+4}. \tag{29}$$

Usually, when a flow model is derived from a given core field model, two other types of errors are considered:

- Observational errors that account for the errors in the Gauss coefficients estimated through the optimization process defined by equation 17.

- A second type of truncation error to account for the fact that short wavelengths of the magnetic field can interact with the short wavelengths of the flow to generate long wavelength secular variation (Eymin and Hulot, 2005).

In the present work, observational errors are not considered because the field and the flow are co-estimated. The second type of truncation errors is also omitted but, in return, we have to impose a rapidly converging spectrum onto the flow. This is not ideal, but it is necessary at this stage, as the field model cannot be efficiently constrained if the flow model has too many degrees of freedom.

3.   Application to CHAMP and observatory data

The methodology described in the previous section has been implemented and applied to a vector data set provided by the CHAMP satellite and 137 observatories. The data set spans approximately one year from 2004.87 to 2005.94 and has been selected using exactly the same selection criteria as for the GRIMM field model (Lesur et al., 2008). These can be summarized as:

- Only vector data are used.

- The data are selected for quiet magnetic conditions.

- High-latitude three component vector data are selected at all local times.

- Mid- and low-latitude data are selected along the X and Y Solar Magnetic (SM) directions during night times.

With such a selection process the data set combines 35975 X and Y (SM) satellite data at mid and low latitudes, 65147 satellite vector data over polar regions, 38954 X and Y (SM) observatory data at mid and low latitudes, and finally 13974 observatory vector data at high latitudes. Gaps in the satellite data distribution are seen at high latitudes due to the blinding of one of the CHAMP star cameras by the sun, whereas at mid and low latitudes they are due to the local time selection applied to minimize the contribution of the ionospheric field in vector data. Observatory data present no gaps over the time period.

The magnetic field contributions modeled are similar to those in GRIMM. The core field model (see equation 5 and 6) is parameterized using SH up to degree 14 and an order 4 polynomial in time (i.e. this is equivalent to order 5 B-splines in between two spline knots). A static internal field is modeled up to SH degree 20, which is enough to avoid aliasing effects in the core field model. The large scale external field is modeled only at SH degree 1, but the modeling is robust only in the X and Y SM directions due to the data selection at mid and low latitudes. As in GRIMM, the time variations of this

large scale external field are parameterized using a piecewise linear polynomial in time with a node every three months. The rapid time variations are parameterized using the VMD (time series of the estimated disturbances due to large scale external fields (Thomson and Lesur, 2007)). Crustal offsets are co-estimated for observatory data in order to account for the unknown contributions from the lithosphere. The high latitude ionosphere field or the toroidal field generated by Field Aligned Currents (FAC) are not considered in the modeling. Again further details can be found in Lesur et al. (2008).

The model parameters are estimated by fitting the data set, either in the least squares sense (i.e. using an L_2 measure of the misfit to the data), or using a reweighted least squares algorithm and an L_1 measure of the misfit to the data (Farquharson and Oldenburgh, 1998). With the data set spanning only one year, the model parameterization described above is much too complex to be derived without regularization, but it is well suited to test how the constraints applied to the flow affect the field model. Several types of constraints are introduced:

- A model is built (hereafter the USN-model) using the usual approach that consists of minimizing simultaneously the data misfit and a measure of the model roughness in time at the CMB. Here we use:

$$\lambda_{1U} \int_{\mathcal{T}} \int_{\Omega} |\partial_t B_r|^2 d\omega \, dt + \lambda_{2U} \int_{\mathcal{T}} \int_{\Omega} |\partial_t^2 B_r|^2 d\omega \, dt \tag{30}$$

where λ_{1U} and λ_{2U} have to be adjusted in order to build a realistic model.

- Two further series of models are built using the approach described in the previous section. They differ by the measure used to minimize the flow complexity in space: either equation 21 (hereafter the BSN-model series) or equation 22 (hereafter the WSN-model series). In both models, equation 23 is minimized to guarantee temporal smoothness of the flow.

4. Effect of the regularization on the co-estimated field and flow models

In this section we compare and discuss the choice of regularization for the co-estimation of the core magnetic field and flow models. All results presented in this section are for the BSN models and are obtained using an L_2 measure of the data misfit. This measure does not lead to the best solutions but is sufficient to understand the response of the model solutions to the constraints applied to the inversion process. The results obtained using an L_1 measure of the misfit require much longer computation time, and are therefore derived only for a limited small set of damping parameters. Such results are presented in the next section.

As noted before, even if the data set consists only of magnetic vector components, the inverse problem for the BSN models is non-linear due to the co-estimation of the core and flow models. An initial guess is therefore required. This initial guess is built from the USN-model and an associated flow model derived through a standard flow inversion using equation 15. The solution of the iterative process is accepted when two successive models of the flow are not significantly different.
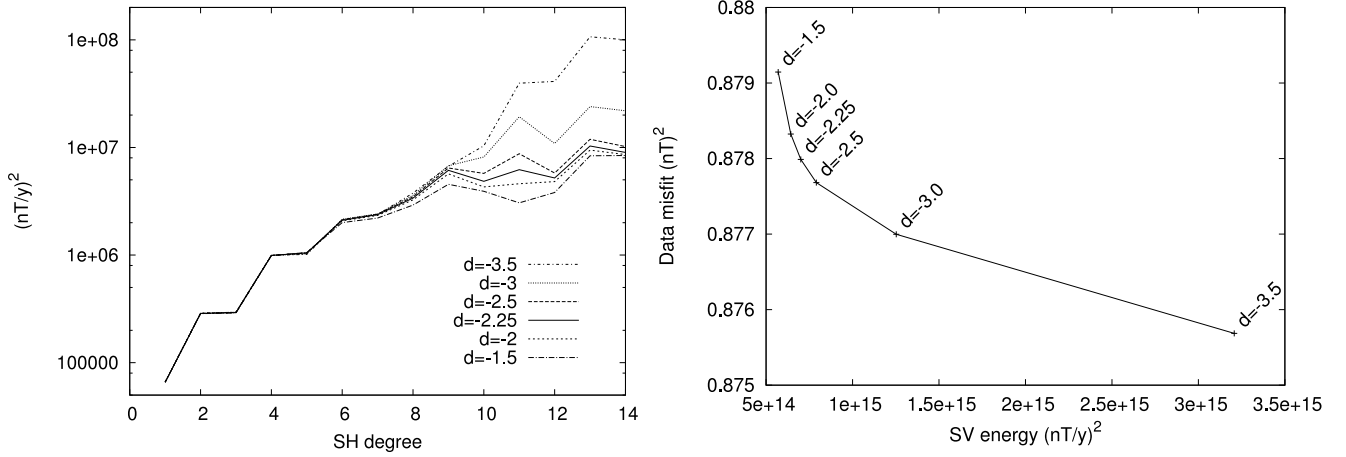
Fig. 2. Left: Evolution of the SV-BSN spectrum at the core-mantle boundary depending on the damping parameter value: $\lambda_{2B} = 10^d$. Right: Trade-off curve between a measure of the SV energy and a measure of the misfit to the data. The labels on the points give the corresponding values of the damping parameter: $\lambda_{2B} = 10^d$.

Such a stable solution is obtained in less than twenty iterations and the final solution is close enough to the starting models for no local-minima to be observed. When started too far from the final solution, we observe that the iterative process simply diverges. In this work we expect the core field model to be a solution of the FF-equation, i.e. the damping parameter λ_1 in equation 20 is set to a relatively large value $\lambda_1 = 10^{-3}$. To estimate quantitatively how well the derived model respects the FF-hypothesis we define the dimensionless ratio ϱ by:

$$\varrho = \frac{\Phi_1}{\sum_{t_i} \mathrm{w}_i^t \, (\dot{\boldsymbol{\Psi}}(t_i) \cdot \mathbf{g})^{\mathrm{T}} \cdot \mathbf{W}^{\dot{g}} \cdot (\dot{\boldsymbol{\Psi}}(t_i) \cdot \mathbf{g})} \tag{31}$$

where Φ_1 is defined in equation 18 and the denominator is just the same quantity Φ_1 derived for a null flow vector $\mathbf{u}$. By testing different models, we observed that for models parameterized with order 4 polynomials in time and spanning only one year, any value of ϱ smaller than 10^{-9} correspond to models in good agreement with the FF-hypothesis

We consider first the effect of minimizing the complexity of the flow at relatively high spherical harmonic degrees. This is achieved by setting the λ_{2B} value in equation 21, successively to $10^{-3.5}$, 10^{-3}, $10^{-2.5}$, $10^{-2.25}$, 10^{-2} and $10^{-1.5}$. The value of λ_3 in equation 23 is set to the *ad hoc* value $10^{4.25}$. The resulting power spectra of the SV at the CMB for year 2005.4 are plotted in Figure 2 for all these λ_{2B} values. As the data set spans only one year, and because only the L_2 norm solution is calculated, the SV is resolved robustly only up to the SH degree 9. However, it is clear that the variation of λ_{2B} affects all the higher SH degrees of the spectra. This is in contrast with the static core field that is not significantly affected by the smoothing constraint. Therefore, as a consequence of imposing the FF-approximation, constraining the flow to get a convergent spectrum directly affects the SV as long as the static part of the core field model is robustly estimated.

Figure 3 presents the evolution of the power spectrum of the toroidal and poloidal flows as a function of the λ_{2B} values. The chosen value has to be larger than or equal to 10^{-3} for the flow to present a clearly converging spectrum. The value
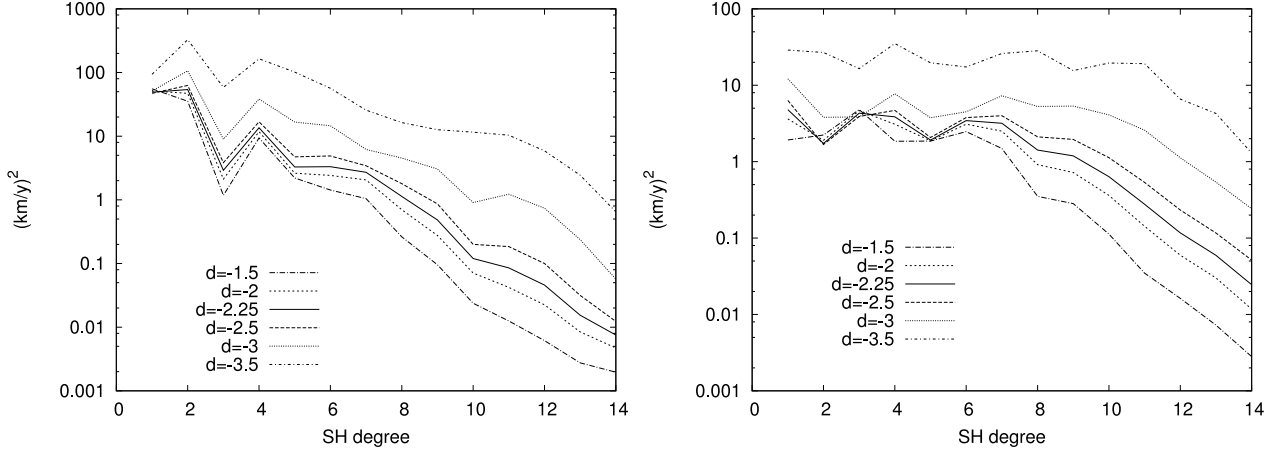
Fig. 3. Evolution of the toroidal (left) and poloidal (right) flow power spectra depending on the damping parameter $\lambda_{2B} = 10^d$.

$\lambda_{2B} = 10^{-1.5}$ is too large and leads to a significant increase in the misfit to the data. Discriminating between the three remaining acceptable λ_{2B} values is rather difficult. We choose here the value $\lambda_{2B} = 10^{-2.25}$. For this value, the spectra of the toroidal and poloidal flows are convergent and the model is compatible with the FF-hypothesis ($\varrho = 0.4\,10^{-15}$). The convergence of the spectrum is fast enough for the possible contributions to the large scale SV of the magnetic field advected by the small scale flow to be very small. This value is also close to the knee of the trade-off curve of SV energy versus data misfit (Figure 2, right). On a data set spanning several years, the SV can be more robustly defined and it is then expected that the regularization affects only the SV for the first and last six months of the model time span.

We now keep the damping parameter λ_{2B} in equation 21 at the value $10^{-2.25}$ and control the changes of the flow in time by varying the parameter λ_3 between $10^{3.5}$ to 10^6. We note that the time variations of the flow are of much smaller amplitude than the flow itself. Therefore, adjusting the damping parameter λ_3 does not affect significantly the flow nor the SV estimates, and the damping parameter λ_{2B} needs no further modifications. Figure 4 gives the power spectra of the static part of the core magnetic field (CF), its SV and its acceleration (SA), for year 2005.4. The spectra are calculated at the Earth's reference radius $a = 6371.2$km and for several values of the damping parameter $\lambda_3 = 10^d$. The curves for the static core field and its SV are given for $d = 4.25$ only, as the power spectra are nearly the same for all the other damping parameter values. The acceleration however changes significantly with λ_3.

In order to understand the behavior of the SA, one has to differentiate in time the radial diffusionless induction equation 4. This leads to:

$$\partial_t^2 B_r = -\nabla_h \cdot (\partial_t U_h \ B_r) - \nabla_h \cdot (U_h \ \partial_t B_r). \tag{32}$$

In the two terms on the Right Hand Side (RHS) of equation 32, we observe that the first strongly dominates the second at the Earth's reference radius. Although the flow amplitude is much larger than its variation in time, this does not balance the difference in amplitude between the magnetic field and its SV. In other words, it is the flow time variations that control most
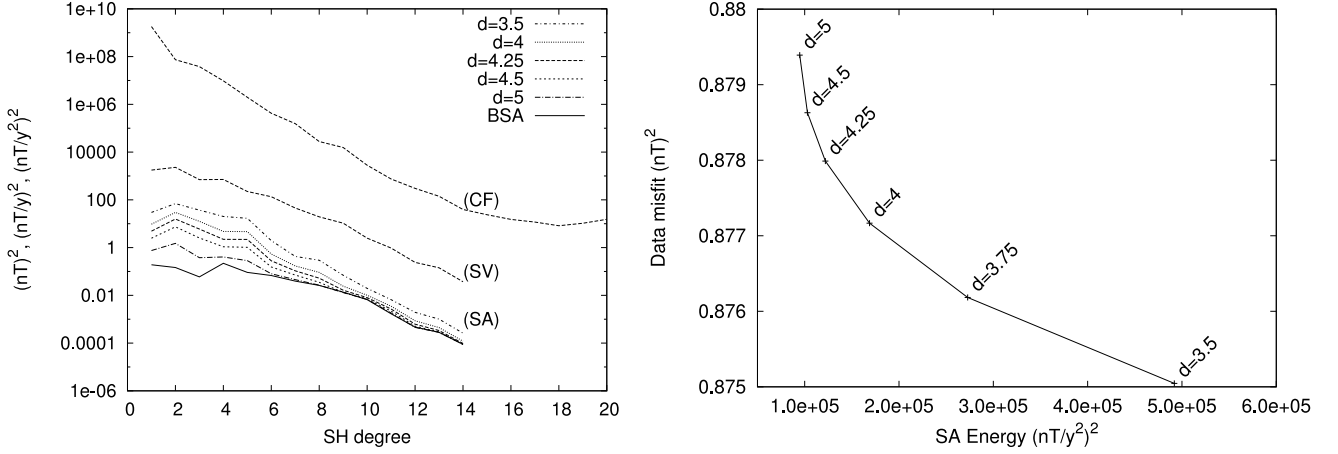
Fig. 4. Left: Evolution of the power spectra of the static part of the core magnetic field (CF), its SV and its acceleration (SA) for different values of the damping parameter: $\lambda_3 = 10^d$. The estimated power spectrum of the background acceleration (BSA) is shown by the solid line. The power spectra are calculated for year 2005.4 at the Earth's reference radius. Right: Trade-off curve between the SA energy and a measure of the misfit to the data. The labels on the points give the corresponding values of the damping parameter: $\lambda_3 = 10^d$.

of the magnetic field acceleration. The SV in the second term on the RHS of equation 32 can be replaced by its expression 4, leading to:

$$\partial_t^2 B_r = -\nabla_h \cdot (\partial_t U_h \; B_r) + \nabla_h \cdot (U_h \; (\nabla_h \cdot (U_h \; B_r))). \tag{33}$$

Obviously, this second term depends only on the field and the flow. Therefore by defining the flow model and imposing the FF-hypothesis, a "background" SA is defined by the second term on the RHS of equation 33, that does not directly depend on the flow temporal variations. A question arises regarding how well this background SA is estimated by the truncated models of the field and the flow derived through the inversion process. To discuss this, two possible effects should be considered:

1) The unknown short wavelengths of the flow and SV can interact to contribute to the large wavelength of the SA. The spectrum of the modeled SV is not convergent at the CMB and therefore this truncation error for the background SA is likely to be significant. However, as for the advection of the short wavelengths of the field by the short wavelengths of the flow, we do not expect this effect to be dominant at small SH degrees. Again, this holds because our flow is essentially large scale and has a convergent spectrum.

2) The flow resolved by the inversion process is only part of the true flow because when advecting the field lines, part of the flow does not contribute to the SV. This hidden flow can nevertheless contribute to the background SA. If we accept the common consensus that the strength of this hidden flow is at most of the same order of magnitude as the modeled flow (see for example Rau et al. (2000) or Asari et al. (2009)), then we can assume that the interaction of the SV with the hidden flow is not larger than the interaction with the modeled flow.
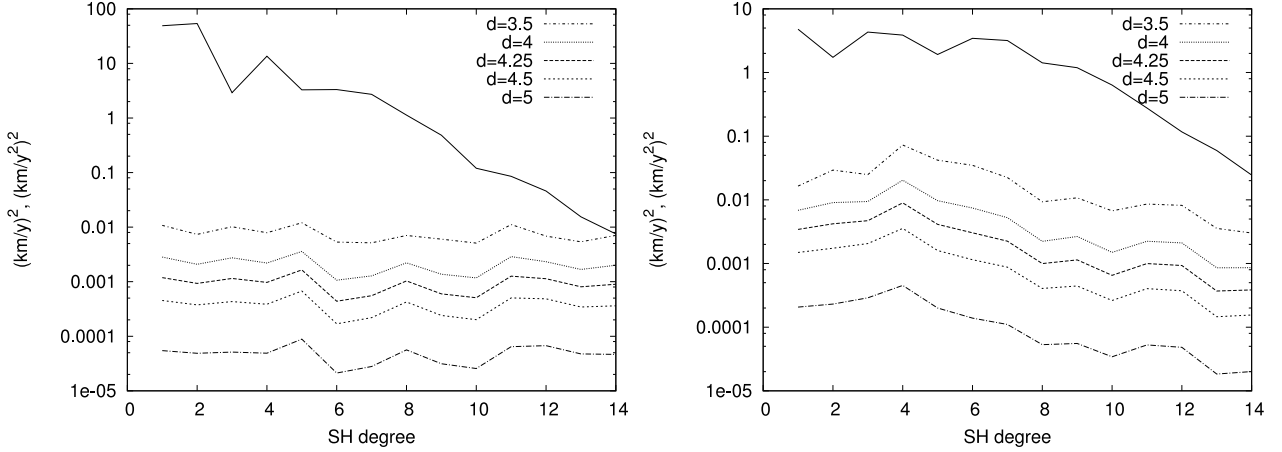
Fig. 5. Evolution of the toroidal (left) and poloidal (right) flow time variation power spectra as a function of the damping parameter $\lambda_3 = 10^d$ for year 2005.4. In both plots, the top solid curve is the static flow spectrum.

Overall, our estimated background SA may not be accurate, but the order of magnitude is acceptable. The power spectrum of the estimated background SA is shown in Figure 4.

It is unlikely that the flow temporal variations are organized such that their associated SA systematically cancels the background SA. Furthermore, the rapidity of the SA evolution, as estimated in core field models like GRIMM and xCHAOS from the energy in their third time derivative, suggests that the flow and its time variations have very different time scales. Therefore, the first and second terms on the RHS of equation 32 are likely to be decoupled. We therefore suggest that, in figure 4, the power spectrum associated with the background SA defines a lower limit of the SA spectrum for a core field compatible with the FF-hypothesis. This is important because it gives us a criterium to test the compatibility of a model with the FF-hypothesis: A core field model with a very steeply decreasing SA spectrum is unlikely to be compatible with the FF-hypothesis.

By strongly damping the flow time variations one may try to reach the limit where only the background SA is significant. This limit was not reached at low SH degrees even for our largest damping value $\lambda_3 = 10^6$ (not shown). At higher SH degrees (i.e. from degree 10 and above) the spectra do not change significantly with the damping value and obviously the solutions get closer to this limit. This difference in behavior depending on the SH degree is simply due to the fact that the data set used does not resolve well the acceleration at high SH degrees.

The plots in Figure 5 show the evolution of the flow time variation spectra as a function of the applied damping. Again, because only one year of data are used, it is relatively difficult to estimate what the best damping parameter value is as the RMS misfit is little affected by a variation of λ_3. We choose here $\lambda_3 = 10^{4.25}$ for the SA energy at small SH degrees to be of the same order as those of the GRIMM and xCHAOS models. This corresponds in Figure 4 right, to a value fairly close to the knee of the damping curve. For the largest damping parameter values ($\lambda_3 > 10^5$), the misfit to data starts to increase

significantly. This confirms that some time variations of the flow are needed to fit the SV data.

5.   Results & Discussions

In this section we present and compare the results obtained using different regularization techniques. All these results were obtained using a L_1 measure of the misfit. The number of iterations before reaching a stable solution is relatively large for such models and data sets: 20 iterations for the USN model and up to 60 iterations for the BSN or WSN models (for the definition of these models refer to section 3).

The USN-model is derived using the regularization parameter $\lambda_{1U} = 10^{-4.5}$ and $\lambda_{2U} = 10^{-0.25}$ in equation 30. It is relatively difficult to set these damping parameter values by examining the trade-off between the fit to the data and the roughness of the solution. We therefore simply set these values such that the power spectra of the model solution, secular variation and acceleration stay reasonably close to those of the GRIMM model. The BSN and WSN models are derived as described in section 4 and the chosen damping parameter values are $\lambda_1 = 10^{-3}$, $\lambda_3 = 10^{4.25}$ for both models and $\lambda_{2B} = 10^{-2.25}$, $\lambda_{2W} = 10^{-0.5}$ for BSN and WSN respectively (see equations 21, 22, 23). The data misfits for these three models are given in table 1 together with the number of data. For all three models, the fit to the data is good at mid and low latitudes but degrades closer to the poles. This is to be expected, because of the chosen data selection criteria. For comparison table 1 also gives the fit to the same satellite data set for the GRIMM model with its lithospheric component truncated at SH degree 20. Not surprisingly, at mid and low latitudes the fit for the GRIMM model is slightly worse than for the other three models, because it was built on much larger time span data set.

In Figure 6, the power spectra of the static core field (CF), SV and SA for the four models GRIMM, BSN, USN, WSN, are compared. All these power spectra are calculated at the Earth's reference radius $a = 6371.2$km and for year 2005.4. All four models have a static part (CF) with very similar power spectra. These cannot be distinguished and only the GRIMM model is displayed.

The GRIMM model presents a SV with slightly less power from SH degrees 6 to 8, explained by the fact that GRIMM is built on a different data set and is smoothed in time. SV-BSN and SV-WSN models are essentially the same. They have very similar power spectra and the power spectrum of their differences never exceeds 0.08(nT/yr)^2. Similarly, the power spectrum of the differences between the SV-BSN (or SV-WSN) model and the associated SV estimated through the FF-equation (i.e. the SV generated exclusively from the advection of the field lines by the flow) never exceeds $5.0 \ 10^{-10}$(nT/yr)^2 in 2005.4. The ratio ϱ, defined in equation 31, is $0.9 \ 19^{-15}$ for the BSN model and $0.2 \ 19^{-14}$ for the WSN model. Therefore, the models built follow (not exactly but very closely) the FF-hypothesis. As expected, due to the regularization technique employed, these two SV models can be downward continued to the CMB without further regularization. The SV-USN model is clearly dominated by the regularization above SH degree 10. Its power drops excessively rapidly from SH degrees

Table 1. Mean (M) and root mean-squares (SD) misfit values for all data types and core field models, in nT. (SM) stands for Solar-Magnetic and H.lat for High-Latitudes

| Data types	Number of data	USN		BSN		WSN		GRIMM	
		M	SD	M	SD	M	SD	M	SD
Sat. X (SM)	35975	-0.50	3.49	-0.51	3.50	-0.51	3.50	-0.68	3.60
Sat. Y (SM)	35975	-0.68	3.71	-0.69	3.71	-0.69	3.71	-0.75	3.75
Sat. X H. lat	65147	1.36	47.08	1.37	47.08	1.37	47.08	0.30	46.97
Sat. Y H. lat	65147	-2.68	51.48	-2.67	51.49	-2.67	51.49	-2.71	51.53
Sat. Z H. lat	65147	-0.95	20.54	-0.93	20.57	-0.94	20.56	-0.74	20.95
Obs. X (SM)	38954	-0.06	3.25	-0.06	3.25	-0.06	3.24	-	-
Obs. Y (SM)	38954	-0.08	3.24	-0.10	3.23	-0.10	3.23	-	-
Obs. X H. lat	13974	-3.72	27.78	-3.91	27.85	-3.89	27.84	-	-
Obs. Y H. lat	13974	-0.15	13.53	0.17	13.57	0.17	13.56	-	-
Obs. Z H. lat	13974	-0.59	20.88	0.63	20.94	0.62	20.94	-	-
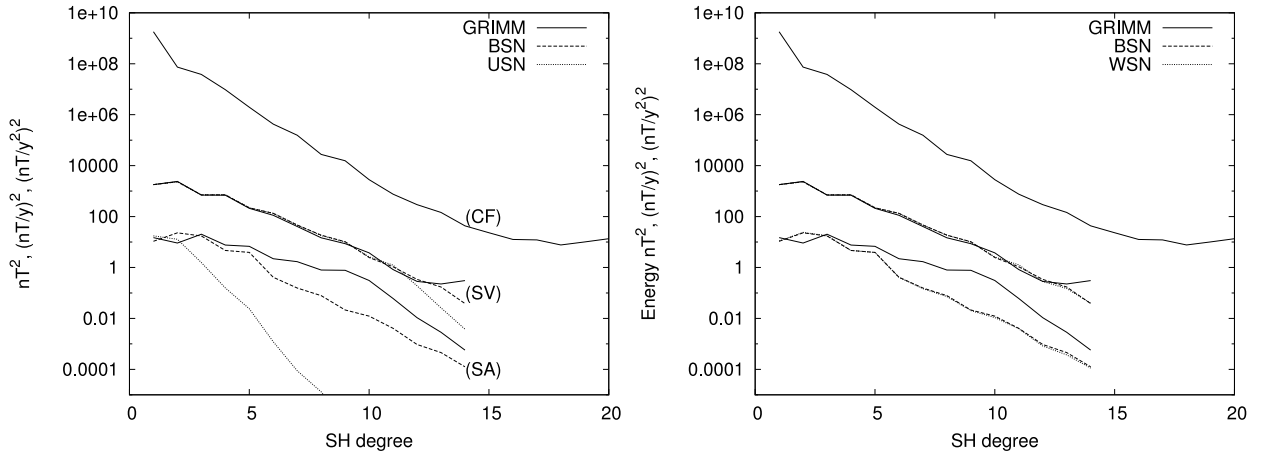
Fig. 6. Power spectra at $a = 6371.2km$ for the static core field (CF), SV and acceleration (SA) for the four models: GRIMM, BSN, USN, WSN. Spectra are computed for year 2005.4

11 to 14.

Figure 7 displays the vertical down component of the SV at the CMB ($c = 3485km$) for both the GRIMM and BSN models. The GRIMM model is truncated at SH degree 12 because, for higher degrees, it contains signal that cannot be attributed to the core. BSN presents stronger SV in some areas. By experimenting with different truncation degrees, we
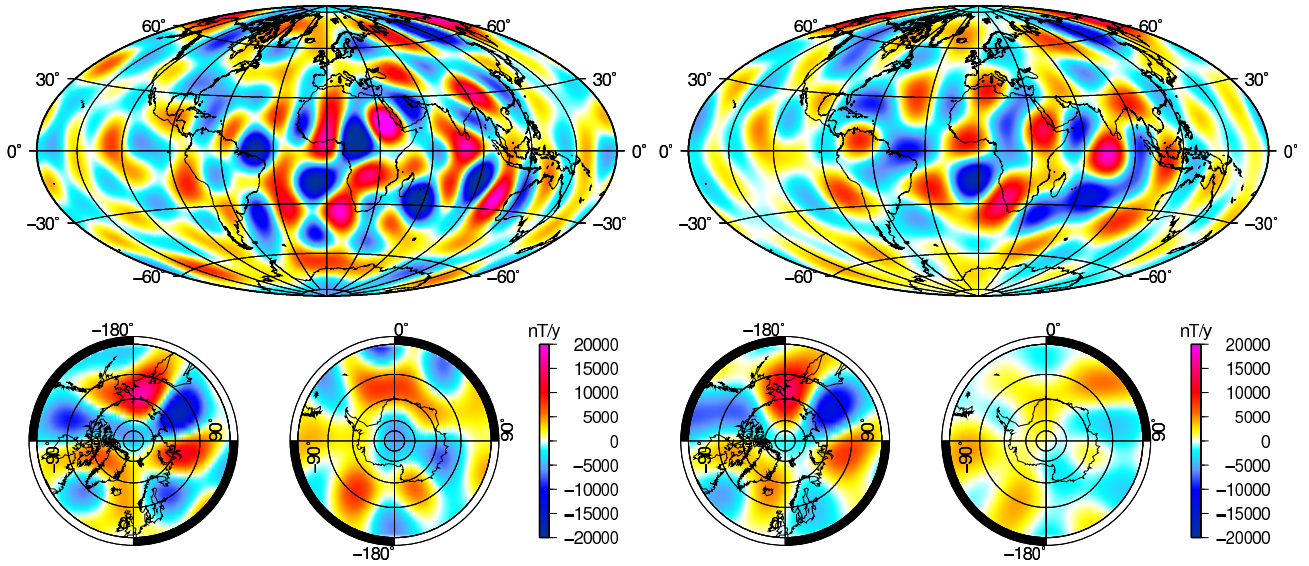
Fig. 7. Maps of the vertical down component of SV at the core-mantle boundary from the BSN-model up to SH degree 14 (left) and GRIMM up to SH degree 12 (right). Maps are calculated for year 2005.4

observed that under Asia and Indian ocean, this is due to the SH truncation degree, whereas under Africa and Antarctica it may be attributed to the slightly better fit to the data set. Under western Atlantic at mid latitudes, the SV power in GRIMM has slightly shifted to higher degrees in BSN. Around the Northern Pole, the GRIMM characteristic alternating positive and negative SV patches along longitudes are slightly more pronounced in BSN. This is partially due to the higher truncation SH degree, but is also enhanced by the regularization process. Because of the core static field shape in these area, such patterns can be easily explained by a flow circulating around the pole that advects the field lines. It is remarkable that the SV for BSN (and WSN) does not present obvious spurious patterns. In particular East-West oscillations near the dip equator, similar to the well known Backus effect, are not present as is generally the case for high spherical harmonic SV models (Wardinski et al., 2008).

The SA models power spectra, in figure 6, are significantly different. As described above, the damping parameter values of the BSN, USN, WSN models have been adjusted such that all SA power spectra match around SH degree 1. From there, the SA-BSN and SA-WSN power spectra stay more or less constant up to SH degree 3 and then drop regularly down. As discussed in section 4, the SA-BSN and SA-WSN power spectra presented here for SH degree higher than 8, are the lowest possible for the models to be compatible with the FF-hypothesis. The behavior of the SA-USN model is clearly anomalous and it shows that the selected data set over a single year does not resolve well the acceleration. It is also clear that the integrals defined in equation 30 impose constraints on the high SH degree of the SA-USN model that are too strong, leading to an unrealistic decrease in the spectrum. Such a model is not compatible with the FF-hypothesis (see discussion in section 4). We see immediately the effect of using the new approach for regularizing the magnetic field inversion process:
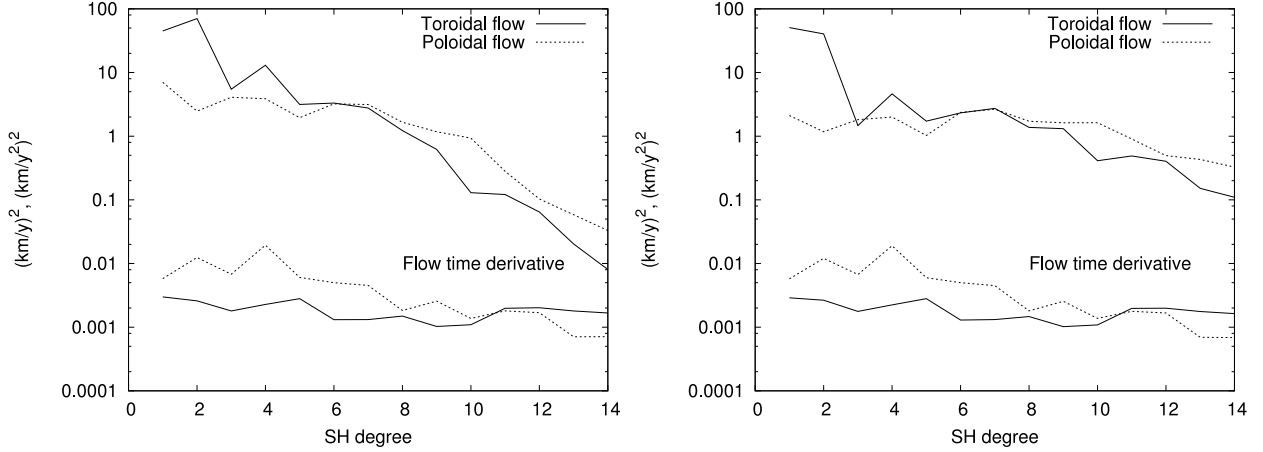
Fig. 8. Power spectra of the flows at the core-mantle boundary ($c = 3485km$) for year 2005.4 computed from the BSN flow model (left), and the WSN flow model (right).

the time behavior of the field model is consistent with the underlying physical process described by the FF-equation and advection is favored as a possible source of the SV. The spectrum of the SA for GRIMM is above the others for degrees 3 to 9. This does not necessarily mean that this spectrum is too high. As stated above, one year of data is not enough to resolve well the SA and by accumulating data over several years, the spectra from both the BSN and WSN model accelerations would possibly rise. However, above SH degree 9 the GRIMM SA is controlled by the applied regularization and probably drops too rapidly to be consistent with the FF-hypothesis.

The SA obtained through our inversion process is only valid for the first two or three SH degrees. Most of the SA patterns observed in the GRIMM model correspond to the SH degree 4 or 5. These SH degrees are not resolved here. We observe however, that the BSN and WSN SA models can be downward continued to the CMB without further regularization. There, they are dominated by their short wavelengths, and the patterns, mainly controlled by the FF-equation, are associated with strong gradients of the SV model (maps of the SA are not shown here).

Figure 8 shows the power spectra of the toroidal and poloidal flows from the BSN and WSN models and also the power spectra of the flow temporal variations. The BSN and WSN flow model spectra differ mainly in their high SH degrees. As expected the BSN has less power than WSN there, whereas, for SH degrees around 4, it is the power spectrum of the WSN model that is the lowest. Although the WSN and BSN flow models are different, the SV corresponding to these models are nearly the same. Indeed one could impose constraints in order to build a flow model with specific and more realistic properties (e.g. tangential geostrophy, pure toroidal flow) leading to similar SV models, but that is not our goal here. The two flows obtained here have similar statistics: The BSN (resp. WSN) has a Kinetic Energy (KE) of 175.13 (km/yr)^2(resp. 128.26 (km/yr)^2). Its toroidal component represent 82.88% (resp. 84.25%) of the KE and the geostrophic component represents 78.55% (resp. 77.58%) of the KE.
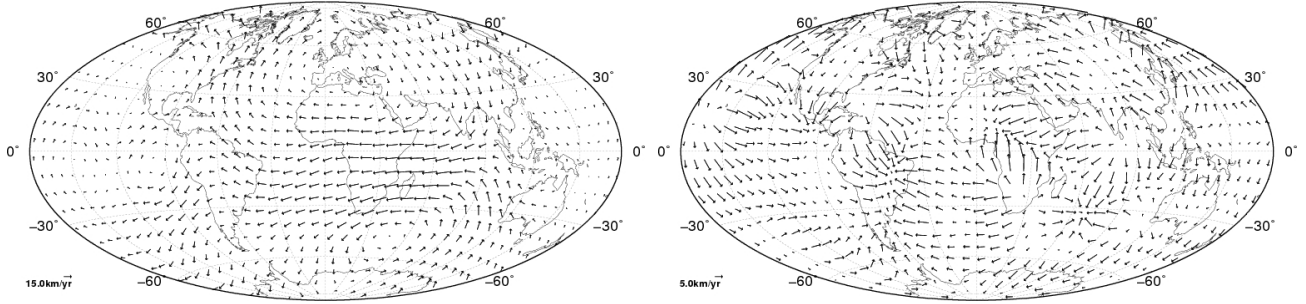
Fig. 9. Maps of the toroidal flow (left) and poloidal flow (right) obtained from the BSN flow model for year 2005.4. Note that the scale is three times

   larger for the poloidal flow.

The BSN flow model is plotted in Figure 9. The toroidal flow that dominates the general flow is remarkably smooth,

but sufficiently complex to advect a core field model leading to a realistic SV model. Some attempts have been made to

minimize further the poloidal component of the flow, but, these led to a degraded fit to the data set. The visual aspect of the

WSN flow is similar to that of the BSN flow.

6.   Conclusions

We derived a core magnetic field model spanning the 2004.87-2005.94 period from CHAMP satellite and observatory

data. The field model is co-estimated together with a model of the flow at the top of the core and we impose the constraint that

the field model closely follows the FF-hypothesis continuously in time. Despite the shortness of the data time span, the SV

model is surprisingly accurate around 2005.4. Similarly the SA model can be resolved for the first SH degrees. However,

our main point in this work has been to investigate how well a core field model inversion process can be regularized by

constraints applied on the co-estimated flow model. In this respect, the results are very encouraging. First, we have shown

that imposing a convergent spectrum on the flow immediately constrains the secular variation such that it can be downward

continued without further regularization to the CMB. Second, we have shown that smoothing temporal variations of the flow

affects the magnetic field acceleration magnitude.

In addition, we have seen that at the Earth's surface the observed SA is mainly controlled by the temporal flow variations.

We suggest that the background SA, that does not depend directly on the flow variations, defines a lower limit of the

acceleration power spectrum for the core field compatible with the FF-hypothesis. Then, if the spectrum of a core magnetic

field model acceleration falls below this limit, the time behavior of this field model is inconsistent with the FF-hypothesis.

Deriving flow time variation information from such an anomalous model would be unlikely to lead to acceptable results.

It would be interesting to test these hypotheses in a dynamo simulation where the induction equation is solved in a self-

consistent manner.

In the approach used, the core flow model is truncated at relatively small SH degrees and, even if the flow has a rapidly

converging spectrum, the interactions between the small scales of the field and the flow could be better accounted for. However, it is not straightforward in the presented framework. This will have to be investigated in a forthcoming study.

Diffusion necessarily exists and one could argue that imposing the FF-hypothesis constraint is not a valid approach at these timescales. We think nevertheless, that to impose the constraint is definitively an approach worth studying. Further, we observe that even under the flow constraints presented above, the error in equation 15 stays very small. Therefore, it is fairly easy to build a model respecting the FF-hypothesis, although that is not a sufficient condition to make the hypothesis valid. Some preliminary work has been done to apply the technique on data sets covering longer time span. There are no apparent serious further difficulties. However, this has to be investigated in detail in future work.

Appendix A. The Field-Flow time parametrisation inconsistency

In this appendix it is shown that the system of equations 15, derived from the diffusion-less induction equation does not have an exact solution if the basis functions $\psi_i(t)$ are algebraic polynomials in time. Indeed, we know that there is no exact solution to equation 15 because the exclusion rules of the Gaunt and Elsasser integrals are such that the linear system is overdetermined; a solution can be obtained only by least squares. In practice, this solution is non-unique because some of the equations are severely under-weighted (sometimes simply ignored) as the SV is unknown at high SH degrees. However, we want to make clear that also in time, using truncated algebraic polynomial series as basis functions leads to solutions that can be only approximations of the exact solution. Rather than using equation 15, we start from the system 16 and re-write in a more general case:

$$\partial_t P(t) = (Q_0 + Q_1 t + Q_2 t^2 + \cdots + Q_m t^m) P(t), \quad P(0) = I \tag{A.1}$$

where the function $P(t)$ corresponds to the magnetic field coefficients and the series $(Q_0 + Q_1 t + Q_2 t^2 + \cdots + Q_m t^m)$ stands for the $A_u(t)$ matrix that we expand as an algebraic polynomial in time in order to describe the flow time variations. The full proof for the general case is outside the scope of this manuscript [1]. We rather address here the simple case where only a dependence in t^{j-1} is considered.

The full proof for the general case can be obtained from the authors

We look for polynomial solutions of the following equation

$$\partial_t P(t) = Q_{j-1} t^{j-1} P(t). \tag{A.2}$$

where Q_{j-1} is a $n \times n$ dimensional matrix. If λ and η are an eigenvalue and the corresponding eigenvector of the matrix Q_{j-1}, then the vector:

$$P(t) = e^{\lambda \frac{t^j}{j}} \eta, \tag{A.3}$$

satisfies the equation A.2. If all real or complex eigenvalues of Q_{j-1} are distinct (with multiplicity 1), then the fundamental solution of A.2 is a linear combination of vectors of the form A.3. In order to obtain a polynomial solution of equation A.2, we must consider the case where $\lambda = 0$ is the only eigenvalue of Q_{j-1} and therefore has multiplicity n.

If λ is an eigenvalue of Q_{j-1} with multiplicity n, we need to find n linearly independent solutions of A.2. In this case the following result holds.

Theorem 1 *If λ is an eigenvalue of Q_{j-1} with multiplicity n, then every solution $P(t)$ of equation A.2 has the form*

$$P(t) = C_1 P_1(t) + C_2 P_2(t) + \cdots + C_n P_n(t),$$

where

$$P_1(t) = e^{\lambda \frac{t^j}{j}} \eta_1, \ \ (Q_{j-1} - \lambda I)\eta_1 = 0,$$

$$P_2(t) = \frac{t^j}{j} e^{\lambda \frac{t^j}{j}} \eta_1 + e^{\lambda \frac{t^j}{j}} \eta_2, \ \ (Q_{j-1} - \lambda I)\eta_2 = \eta_1,$$

$$\cdots \ \cdots$$

$$P_n(t) = \frac{t^{j(n-1)}}{j(n-1)} e^{\lambda \frac{t^j}{j}} \eta_1 + \frac{t^{j(n-2)}}{j(n-2)} e^{\lambda \frac{t^j}{j}} \eta_2 + \cdots + e^{\lambda \frac{t^j}{j}} \eta_n, \ \ (Q_{j-1} - \lambda I)\eta_n = \eta_{n-1}.$$

It is easy to check by direct substitution that the vectors $[P_1(t), P_2(t), \ldots, P_n(t)]$ satisfy the equation A.2. They are also linearly independent and therefore form a fundamental set of solutions.

Since we are interested in polynomial solutions of equation A.2, it is clear that they can be obtained only if $\lambda = 0$. Having all eigenvalues equal to zero is a very restrictive requirement that is not relevant for the problem we are considering here. We therefore conclude that an algebraic polynomial expansion for the time representation should not be used for both the magnetic field and flow models in order to obtain exact solutions to the system of equations 15.

References

Asari, S., Shimizu, H., and Utada, H. (2009). Robust and less robust features in the tangential geostrophy core flows. *Geophys. J. Int.*, 178(2):678–692.

Beggan, C. D. and Whaler, K. A. (2009). Forecasting change of the magnetic field using core surface flows and ensemble kalman filtering. *Geophys. Res. Lett.*, 36(18).

Bloxham, J. (1988). The determination of fluid flow at the core surface from geomagnetic observations. In Vlaar, N. J., Nolet, G., Wortel, M. J. R., and Cloetingh, S. A. P. L., editors, *Mathematical Geophysics, A Survey of Recent Developments in Seismology and Geodynamics*, pages 189–208. Reidel, Dordrecht.

Bloxham, J. and Gubbins, D. (1986). Geomagnetic field analysis. IV - Testing the frozen-flux hypothesis. *Geophys. J. Roy. Astron. Soc.*, 84:139–152.

Eymin, C. and Hulot, G. (2005). On core surface flows inferred from satellite magnetic data. *Phys. Earth Planet. Inter.*, 152(3):200–220.

Farquharson, C. and Oldenburgh, D. (1998). Non-linear inversion using general measures of data misfit and model structure. *Geophys. J. Int.*, 134:213–227.

Fournier, A., Eymin, C., and Alboussière, T. (2007). A case for variational geomagnetic data assimilation: Insights from a one-dimensional, non-linear, and sparsely observed MHD system. *Nonlinear processes Geophys.*, 14(3):163–180.

Gillet, N., Pais, M., and Jault, D. (2009). Ensemble inversion of time-dependent core flow models. *Geochem. Geophys. Geosyst.*, 10(Q06004).

Holme, R. (2007). Large-scale flow in the core. In Olson, P., editor, *Treatise on Geophysics*, volume 8. Elsevier Ltd., Amsterdam.

Jackson, A. (1997). Time-dependency of tangentially geostrophic core surface motions. *Phys. Earth Planet. Inter.*, 103:293–311.

Jackson, A., Constable, C., Walker, M., and Parker, R. (2007). Models of the Earth's main magnetic field incorporating flux and radial vorticity constraints. *Geophys. J. Int.*, 171(1):133–144, doi: 10.1111/j.1365–246X.2007.03526.x.

Jackson, A., Jonkers, A. R. T., and Walker, M. R. (2000). Four centuries of geomagnetic secular variation from historical records. *Phil. Trans. R. Soc. Lond. A*, 358:957–990.

Jault, D. and Le Mouël, J. L. (1991). Physical properties at the top of the core and core surface motions. *Phys. Earth Planet. Inter.*, 68:76–84.

Korte, M. and Constable, C. G. (2004). Continuous geomagnetic field models for the past 7 millennia II: CALS7K.

Geochem., Geophys., Geosyst., 6, Q02H16.

Lesur, V., Macmillan, S., and Thomson, A. (2005). The BGS magnetic field candidate models for the 10th generation IGRF. *Earth, Planets, and Space*, 57:1157–1163.

Lesur, V., Wardinski, I., Rother, M., and Mandea, M. (2008). GRIMM - The GFZ Reference Internal Magnetic Model based on vector satellite and observatory data. *Geophys. J. Int.*, 173.

Liu, D., Tangborn, A., and Kuang, W. (2007). Observing system simulation experiments in geomagnetic data assimilation. *JGR*, 112(B08103):doi: 10.1029/2006JB004691.

Maus, S., McLean, S., Dater, D., Lühr, H., Rother, M., Mai, W., and Choi, S. (2005). NGDC/GFZ candidate models for the 10th generation International Geomagnetic Reference Field. *Earth, Planets and Space*, 57:1151–1156.

Moon, W. (1979). Numerical evaluation of geomagnetic dynamo integrales. *Computer Physics Communications*, 16:267–271.

Olsen, N. (2002). A model of the geomagnetic field and its secular variationfor epoch 2000 estimated from Ørsted data. *Geophys. J. Int.*, 149:454–462.

Olsen, N., Lühr, H., Sabaka, T., Mandea, M., Rother, M., Töffner-Clausen, L., and Choi, S. (2006). CHAOS – A model of the Earth's magnetic field derived from CHAMP, Oersted, and SAC-C magnetic satellite data. *Geophys. J. Int.*, 166(1):67–75.

Olsen, N. and Mandea, M. (2008). Rapidly changing flows in the Earth's core. *Nature Geoscience*, 1(6):390–394.

Olsen, N., Sabaka, T., and Lowes, F. (2005). New parameterisation of external and induced fields in geomagnetic field modelling, and a candidate model for IGRF 2005. *Earth Planets, and Space*, 57:1141–1149.

Rau, S., Christensen, U., Jackson, A., and Wicht, J. (2000). Core flow inversions tested with numerical dynamo models. *Geophys. J. Int.*, 141:485–497.

Roberts, P. H. and Scott, S. (1965). On the analysis of secular variation, 1, A hydromagnetic constraint: *Theory*. *J. Geomag. Geoelectr.*, 17:137–151.

Sabaka, T. J., Olsen, N., and Purucker, M. E. (2004). Extending comprehensive models of the Earth's magnetic field with Ørsted and CHAMP data. *Geophys. J. Int.*, 159:521–547.

Thomson, A. and Lesur, V. (2007). An improved geomagnetic data selection algorithm for global geomagnetic field

modelling. *Geophys. J. Int.*, 169:951–963. doi: 10.1111/j.1365-246X.2007.03354.x.

Voorhies, C. V. and Backus, G. E. (1985). Steady flows at the top of the core from geomagnetic-field models – the steady motions theorem. *Geophys. Astrophys. Fluid Dyn.*, 32:163–173.

Waddington, R., Gubbins, D., and Barber, N. (1995). Geomagnetic-field analysis .5. Determining steady core-surface flows directly from geomagnetic observations. *Geophys. J. Int.*, 122:326–350.

Wardinski, I., Holme, R., Asari, S., and Mandea, M. (2008). The 2003 geomagnetic jerk and its relation to the core surface flows. *Earth and Planetary Science Letters*, 267:468–481.

Whaler, K. A. (1986). Geomagnetic evidence for fluid upwelling at the core-mantle boundary. *Geophys. J. Roy. Astron. Soc.*, 86:563–588.

Whaler, K. A. and Holme, R. (2007). Consistency between the flow at the top of the core and the frozen-flux approximation. *Earth, Planets and Space*, 59:1219–1229.

V.Lesur (e-mail: lesur@gfz-potsdam.de)